



## Shear-wave birefringence and current configuration of converging lithosphere under Tibet

Wang-Ping Chen<sup>a,\*</sup>, Michael Martin<sup>a</sup>, Tai-Lin Tseng<sup>a,b</sup>, Robert L. Nowack<sup>c</sup>,  
Shu-Huei Hung<sup>b</sup>, Bor-Shouh Huang<sup>d</sup>

<sup>a</sup> Dept. of Geology, University of Illinois, Urbana IL 61801, USA

<sup>b</sup> Dept. of Geosciences, National Taiwan University, Taipei, 10617, Taiwan, ROC

<sup>c</sup> Dept. of Earth and Atmos. Sciences, Purdue University, West Lafayette IN 47907, USA

<sup>d</sup> Institute of Earth Sciences, Academia Sinica, Taipei, Taiwan, ROC

### ARTICLE INFO

#### Article history:

Received 17 August 2009

Received in revised form 11 March 2010

Accepted 11 April 2010

Available online 8 May 2010

Editor: T.M. Harrison

#### Keywords:

seismic anisotropy  
collision zone  
continental lithosphere  
Tibet-Himalayas  
Hi-CLIMB

### ABSTRACT

New data from west-central Tibet show that birefringence of *S*-waves has two pronounced increases in magnitude toward the hinterland. Null birefringence persists to about 75 km north of the Indus–Yarlung suture (IYS) between the Indian shield and the Lhasa terrane of southern Tibet. A second, rapid increase occurs about 100 km farther north of the Bangong–Nujiang sutures between the Lhasa terrane and the Qiangtang terrane in central Tibet. The latter feature is consistently observed along three long transects that collectively span a lateral (orogen-parallel) distance of about 600 km and is likely to mark the northern, leading edge of sub-horizontally advancing mantle lithosphere of the Indian shield (the “Greater India”) – an interpretation consistent with the latest results of finite-frequency tomography using both *P*- and *S*-wave travel-times, previous results of modeling gravity anomalies, and a host of other seismic observations. Similarly, complementary constraints indicate that the sudden onset of significant birefringence north of the YYS is likely to be the southern termination of Eurasian mantle lithosphere. Curiously, the shortest of three transects showed null birefringence through much of the Lhasa terrane, a pattern inconsistent with those of He isotopes and gravity.

© 2010 Elsevier B.V. All rights reserved.

### 1. Introduction

Continental collision is a process fundamental to reassembling of super-continent – an on-going process, from the Alps to Papua New Guinea, covering a distance of about 15,000 km. A focal point along this immense chain of active collision is the Tibetan plateau, a unique tectonic feature on the Earth with a great elevation of about 5 km over a vast area of  $3 \times 10^6$  km<sup>2</sup>. The evolution of this massive plateau has been a focus of continual debate since 1924 (Argand, 1924; Yin and Harrison, 2000; Tapponnier et al., 2001). Generally there is a consensus that the plateau is built through a succession of collisions. The most recent episode involves the collision of the Indian shield with the Lhasa terrane of southern Tibet, an event that initiated about 55 Ma ago whose surface trace is the Indus–Yarlung suture (IYS). A previous event, whose surficial expression is the Bangong–Nujiang suture (BNS) between the Lhasa terrane and the Qiangtang terrane in central Tibet, occurred in the Jurassic–Cretaceous time (Yin and Harrison, 2000).

During the past decade, several large-scale projects have been carried out in Tibet to gain better understanding of the dynamics of continental collision (e.g., Tilmann et al., 2003). However, most field deployments concentrated near the main north–south (N–S) trending highway from Yadong to Golmud (profile GT, approximately along the 92°E meridian), leaving a vast region of Tibet unexplored in detail. This skewness in focus, largely constrained by logistics, has been alleviated by Project Hi-CLIMB (Himalayan–Tibetan Continental Lithosphere during Mountain Building) – the first large-scale field experiment to unveil the subsurface geology of central and western Tibet. As the mainstay of Hi-CLIMB, over 200 broadband seismometers were deployed in 2002–2005, including a dense-spaced, N–S trending linear array extending about 800 km, and a regional array with a lateral, east–west (E–W) coverage of about 500 km (Fig. 1).

In the first part of this study, we report new results, from data gathered during Project Hi-CLIMB, of how birefringence of *S*-waves, or transverse seismic anisotropy, varies across the Himalayan–Tibetan collision zone. As a shear-wave propagates through an anisotropic medium, its in-plane and out-of-plane components propagate at different speeds, resulting in differential arrival time (split time,  $\delta t$ ) between the components (shear-wave splitting or birefringence). To ensure that observed birefringence is caused by anisotropy beneath the receiving seismic station, it is common to

\* Corresponding author. Tel.: +1 217 333 2744; fax: +1 217 244 4996.  
E-mail address: [wpchen@illinois.edu](mailto:wpchen@illinois.edu) (W.-P. Chen).

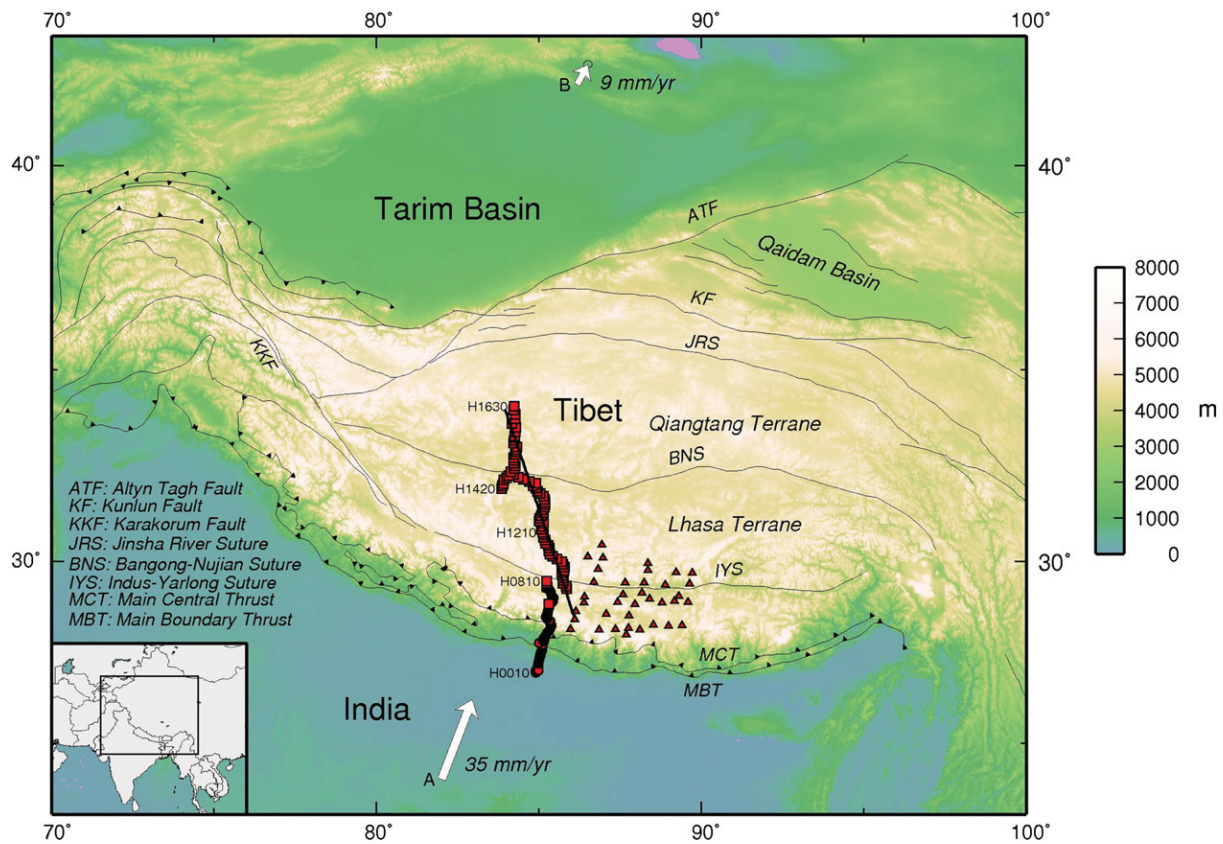


**Fig. 1.** Color-coded topographic map of Tibet, showing all locations of broadband seismic stations deployed during Hi-CLIMB. During the final stage of the deployment, the lateral, regional array (triangles) was deployed at the same time when the majority of the north–south trending linear array north of the MCT (see legend) was operating. Large arrows show current ground velocity with respect to stable Siberia (Sella et al., 2002).

use observations of SKS/SKKS phases. Since they propagate steeply from liquid-to-solid interface of the core–mantle boundary toward the receiver, the initial polarization of SKS/SKKS phases is radial. As such a ray passes through a transversely anisotropic region, characterized by a sub-horizontal axis of symmetry, a single, radially polarized wavelet splits into two orthogonally polarized components of different wave speeds (e.g., Silver, 1996). The cause of birefringence in the upper mantle is generally accepted to be a result of preferred orientation of minerals (mainly olivine) due to finite strain. Two leading candidates for causing petro-fabric are tectonic deformation in the lithospheric mantle and asthenospheric flow below the lithosphere associated with plate motions (e.g., Silver, 1996; Savage, 1999). The latter is unlikely to be applicable to our case because many observations on the Indo–Australian plate showed null splitting, even though it has a uniquely high speed of plate motion in the hotspot frame of reference (Özalaybey and Chen, 1999).

In the second part of this study, we compare results from Hi-CLIMB with those from earlier studies of seismic anisotropy along two profiles located about 500 km farther to the east. In turn, regional patterns of *S*-wave birefringence over this collision zone place important constraints on the current configuration of converging lithosphere under one of the most spectacular tectonic events during the Cenozoic.

## 2. Data, analysis and the Hi-CLIMB transect

Using well-established methodology, the main seismic phases being analyzed are SKS and SKKS waveforms. This procedure has been extensively discussed in the literature. Below we highlight only the most salient points of our data and analysis, and refer readers to

comprehensive reviews for details of methodology (Silver, 1996; Savage, 1999).

We examined data from all large to moderate-sized earthquakes that occurred at depths greater than 70 km and at distances appropriate for SKS/SKKS phases during the entire period of deployment for Hi-CLIMB (late 2002 to late 2005). In all, results from a total of 51 earthquakes are included in the final dataset. The overall range of back-azimuths is wide (about 270°), even though there are some unavoidable gaps due to more-or-less fixed locations of seismicity (Fig. 2).

Fig. 3 shows an example of data recorded in the interior of the Lhasa terrane. In the original data, there is significant signal of SKS phase on the transverse component and its waveform resembles the time-derivative of that on the radial component (resulting in elliptical particle motion, inset of Fig. 3) – telltale signs of large birefringence (Silver and Chan, 1991). Best-fitting values of: (1) The orientation of polarization for the fast-traveling component (fast polarization direction,  $\phi$ ), and (2) differential arrival times (split time or delay time,  $\delta t$ ) between the fast- and the slow-traveling components are determined by grid-search (inset on lower-right of Fig. 3).

Using optimal values of  $\phi$  and  $\delta t$ , waveforms should show no signal above the noise level on the transverse component after correcting for the effect of splitting. Furthermore, after such correction, the particle motions are close to linear (Fig. 3). The corresponding misfit function reflects the amplitude of the corrected transverse component for various trial values of  $\phi$  and  $\delta t$ .

In cases where the results of a grid-search using a single earthquake are not well constrained, instead of directly averaging results from several individual events, we use the technique proposed by Wolfe and Silver (1998) to stack normalized misfit functions from multiple earthquakes recorded by the same station. Fig. 4 shows an

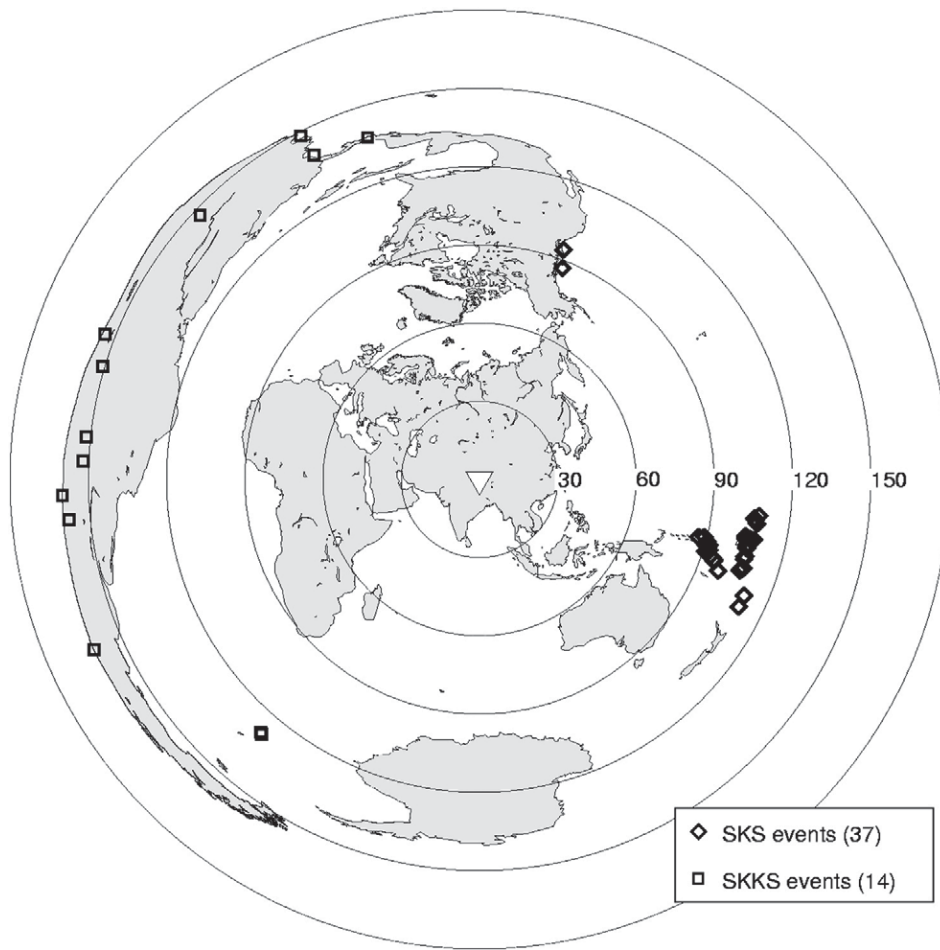


Fig. 2. Map (in azimuthal equidistant projection) showing the distribution of deep- and intermediate-focus earthquakes used for the determination of shear-wave splitting. Data from a total of 51 events were analyzed.

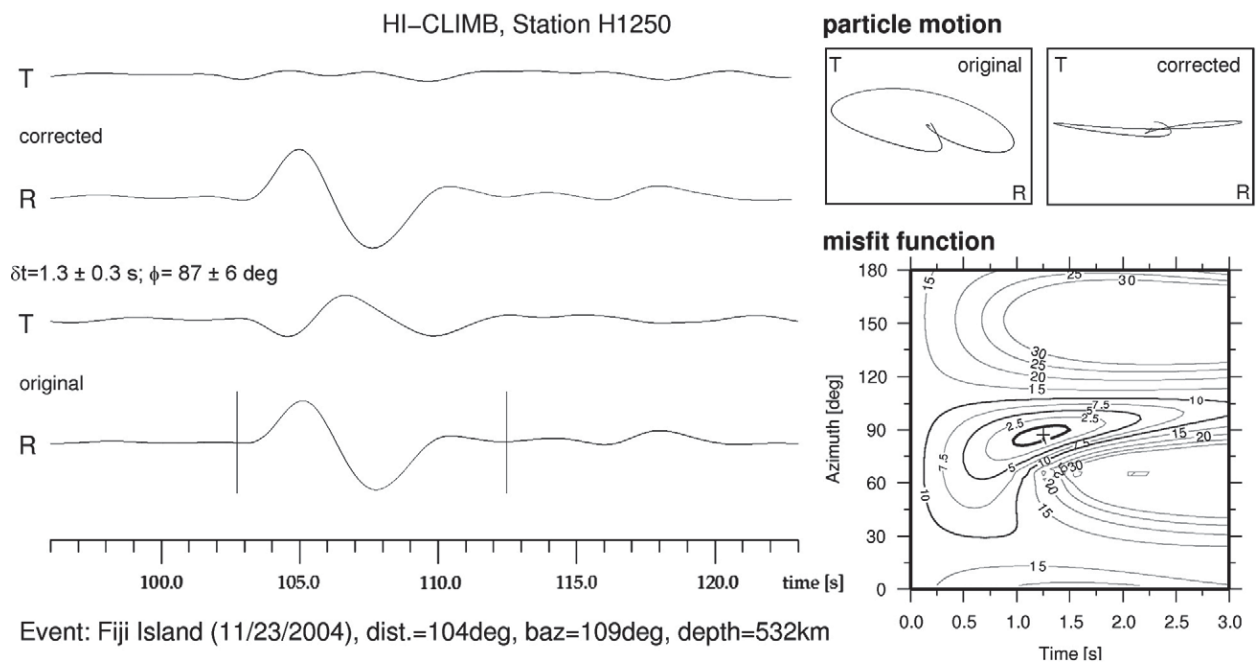
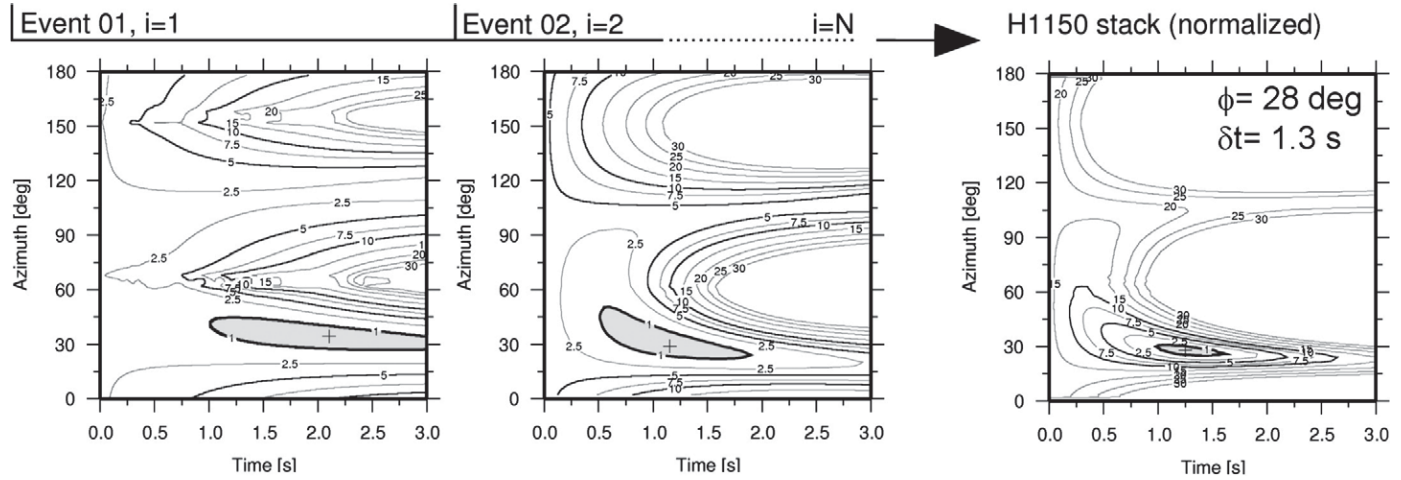
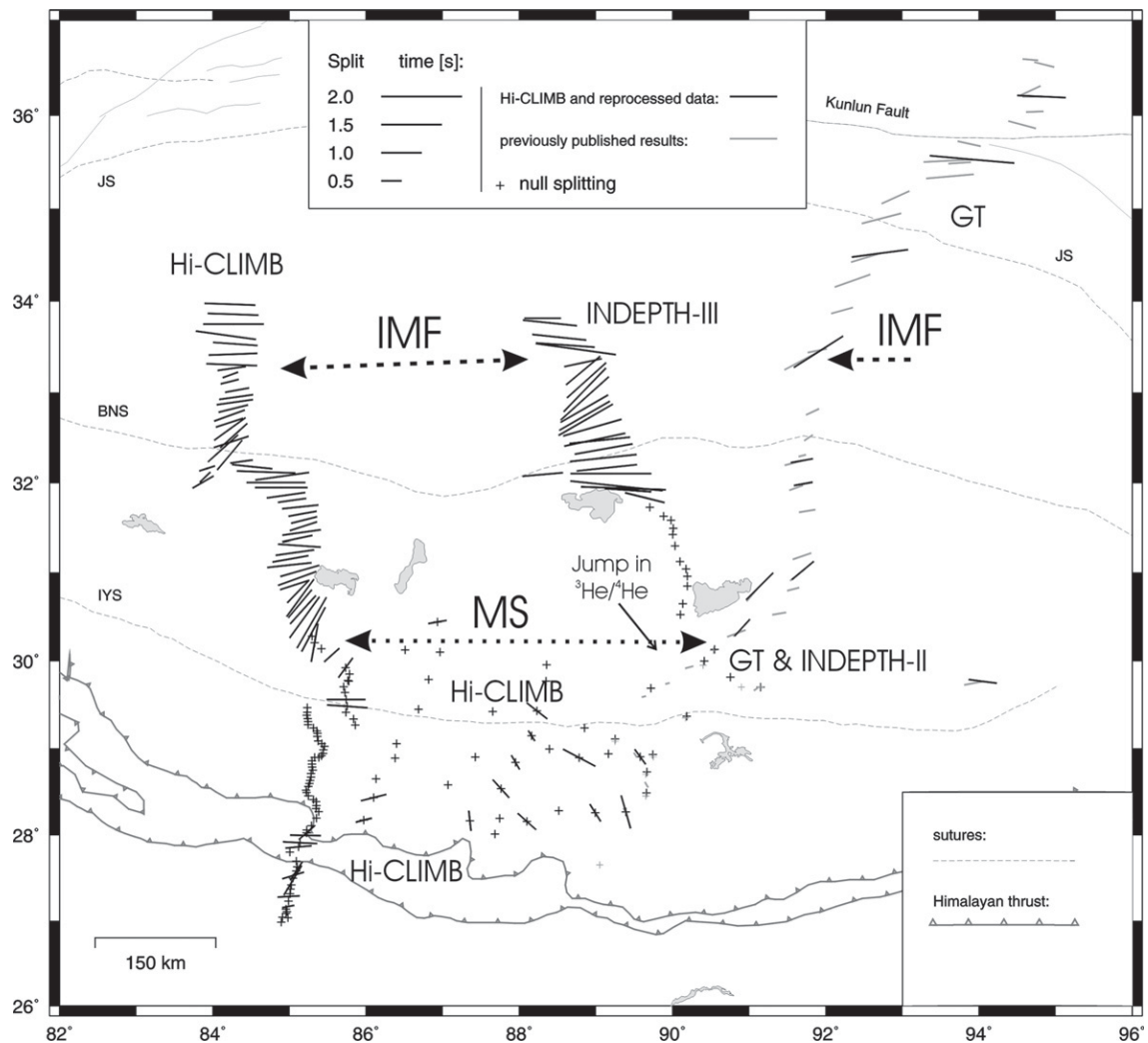


Fig. 3. An example of broadband seismograms (ground velocity filtered between the periods of 5 s and 30 s) showing SKS phase recorded on radial (R) and transverse (T) components at a station in the interior of the Lhasa terrane. Significant signal appeared on the original T-component, a clear indication of transverse seismic anisotropy. After using optimal values determined by minimizing amplitude on the T-component (the misfit function, inset on lower-right) to correct for the effect of anisotropy, no signal above the noise level is left on the T-component and the particle motion changed accordingly from elliptical to linear (inset on upper-right). Vertical bars mark the time-window used in the analysis. In the inset on lower-right, the contour in thick curve marks the overall minimum in misfit (at the 95% level of confidence or two standard deviations under a  $\chi^2$  distribution).

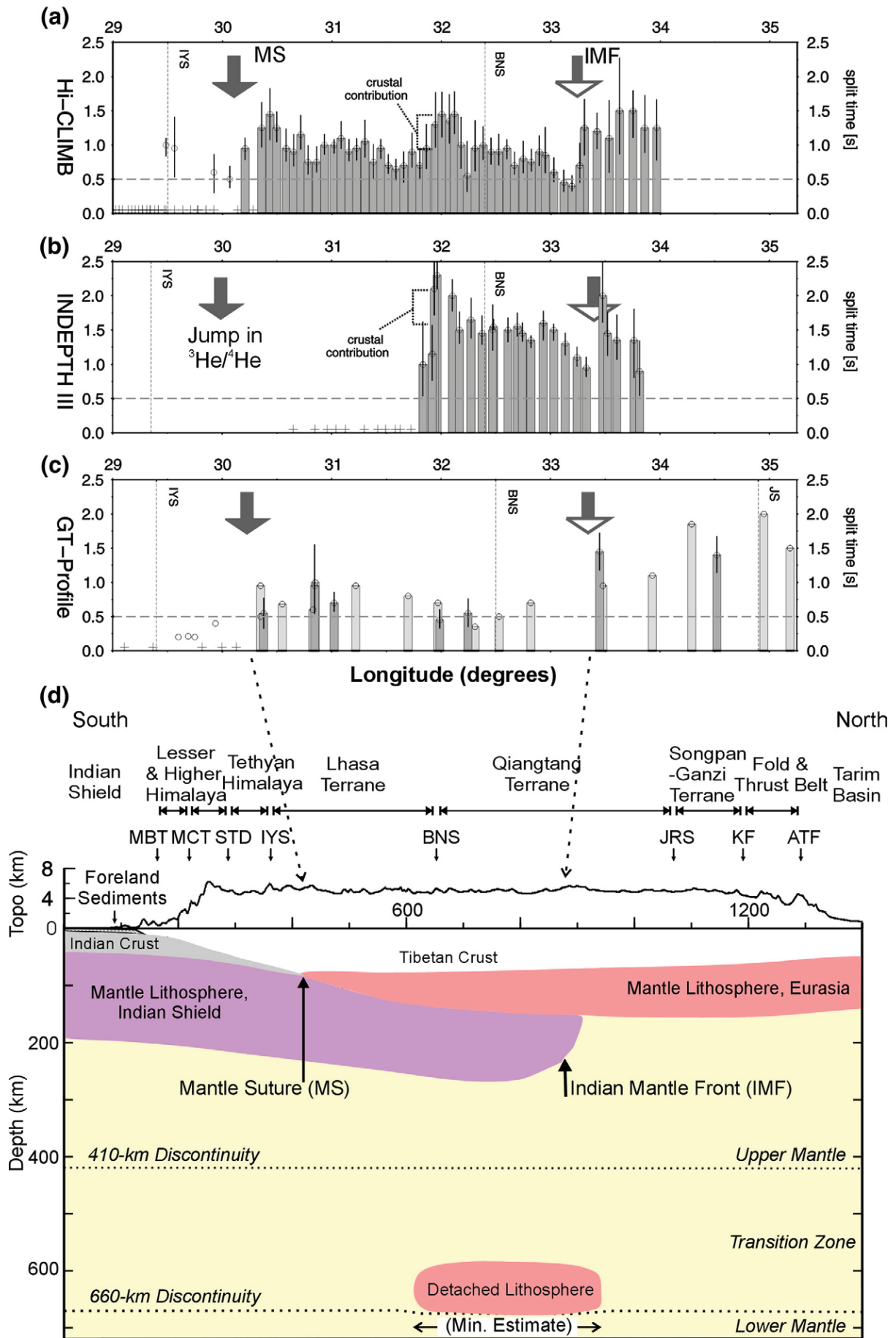


**Fig. 4.** An example of how stacking of normalized misfit functions for different events successively improved estimates of differential arrival times (split time or delay time,  $\delta t$ ) and the fast polarization direction ( $\phi$ ) at a station in southern Lhasa terrane. In this case, a total of 13 events are used.



**Fig. 5.** A map summarizing split times,  $\delta t$ , and fast polarization directions ( $\phi$ ) along three large-scale profiles across Tibet. Arrows mark two salient features that we interpret as (1) the southern limit of the Eurasian mantle lithosphere or the mantle suture (MS), and (2) the leading edge of the Indian mantle lithosphere (IMF); with the latter being apparent along all three profiles. The mantle suture is not covered by the INDEPTH-III profile but is independently identified by an order-of-magnitude drop in the isotopic ratio  $^3\text{He}/^4\text{He}$  (Hoke et al., 2000). A large region of null splitting in the southern part of this plot is independently verified by Fu et al. (2008). Sources of original data appear in Huang et al. (2000), Chen and Özalaybey (1998), and references therein.

**Fig. 6.** (a–c) Comparisons of three large-scale profiles of  $S$ -wave split time ( $\delta t$  in s) across Tibet. For direct comparison, we plotted all three profiles along north–south trends. Key features are marked according to the same layout as in Fig. 5. Open circles are isolated cases of birefringence south of the mantle suture. Measurements with error-bars (and shown in dark grey) are those analyzed by us; otherwise we plot values reported in the literature. The horizontal dotted-line represents the threshold for null birefringence. (d) A schematic cross-section showing the current configuration of the sub-continental lithospheric mantle, including a large-scale anomaly of high  $P$ -wave speed resting on top of the lower mantle and interpreted as the remnant of thickened (and subsequently detached due to Rayleigh–Taylor instability) lithospheric mantle (Chen and Tseng, 2007). The dimension of the detached lithosphere shown is a minimal estimate, limited by current coverage of seismic arrays around Tibet. For reference, we also show key geologic units/boundaries and topography at the present (vertically exaggerated by a factor of 13.15).



example of how stacking using a total of 13 earthquakes considerably narrows the range of estimates for  $\delta t$  which was poorly constrained by data from a single earthquake. Furthermore, there are occasional discrepancies between results from SKS and SKKS phases. In such cases, we rely on results from SKS because the SKKS phase is susceptible to complexities near the core–mantle boundary (Long, 2009). With a few exceptions, errors in our results, at the 95% level of confidence, are generally about 0.3–0.5 s in  $\delta t$  and 10°–20° in  $\phi$ . While azimuthal coverage of data is insufficient to rule out more complex models, analysis using a single anisotropic layer provides satisfactory explanation of observed data.

Figs. 5 and 6a show our results in map-view and cross-section, respectively (also see the Appendix for details). When birefringence is present, the trend of fast polarization is approximately east–west (E–W) to northeast–southwest, with variations that span a range of approximately 45°. Such variations have been noted elsewhere in Tibet and were attributed to effects of strike–slip faulting in the shallow crust which do not contribute significantly to the overall split time,  $\delta t$  (McNamara et al., 1994; Chen and Özalaybey, 1998; Huang et al., 2000).

The magnitude of  $\delta t$ , however, shows two marked changes. The first feature occurs about 100 km north of the IYS where  $\delta t$  increases from null values ( $0.1 \pm 0.1$  s) to an average of  $0.8 \pm 0.3$  s. This stepwise jump in  $\delta t$  coincides with a local minimum in Bouguer gravity anomaly and is along the same regional trend where the isotopic ratio  $^3\text{He}/^4\text{He}$  changes by an order of magnitude (Jin et al., 1996; Hoke et al., 2000). Currently,  $^3\text{He}$  is not being produced near the Earth's surface, so a high ratio of  $^3\text{He}/^4\text{He}$  must reflect degassing deep in the lithosphere or below. Thus three independent observations support the interpretation that the Eurasian mantle lithosphere terminates north of the IYS (Chen and Özalaybey, 1998; Jin et al., 1996; Hoke et al., 2000) (the mantle suture, “MS” in Fig. 5).

Notice that null splitting begins in the southern end of the profile, where the Indian shield is under the sedimentary cover of the foreland basin but yet to be underthrust beneath the Himalayan deformation front, and persists for at least 300 km northward (Fig. 5). As such, not only variations in birefringence along the profile serve as convenient geologic markers, but null splitting of underthrust Indian shield also suggests that the onset of significant anisotropy under Tibet marks the northern terminus of pristine Indian lithosphere that is thrusting under the Himalayan–Tibetan orogen at a rate of about 35 mm/year (Sella et al., 2002). Beyond this terminus, tectonic fabric such as that associated with deforming lithospheric mantle of Eurasia must be present (Chen and Özalaybey, 1998).

Further northward,  $\delta t$  fluctuates between values as low as  $0.5 \pm 0.3$  s to as high as  $1.5 \pm 0.3$  s until just north of the BNS where  $\delta t$  holds steady at a near constant value of  $1.0 \pm 0.3$  s (Fig. 6a). At about 100 km north of the BNS,  $\delta t$  drops markedly to a low of  $0.5 \pm 0.1$  s then quickly jumps to high values of about  $1.3 \pm 0.3$  s to  $1.5 \pm 0.3$  s. This second increase in  $\delta t$  is even more pronounced along profile GT (Fig. 6c) and coincides with another low in Bouguer gravity anomaly where mechanical models of plate flexure indicate the termination of underthrust Indian mantle lithosphere (the Indian mantle front, “IMF” in Fig. 6) (Jin et al., 1996). Along the Hi-CLIMB profile, this interpretation is corroborated by the latest results of travel-time tomography: Combining finite-frequency theory and a data-adaptive, multi-scale parameterization, high-resolution images from both P- and S-wave travel-times consistently show termination of high wave-speeds near the IMF (Hung et al., 2010).

In fact, the latest results by Hung et al. (2010), including the first image from S-waves under western Tibet, show no indication of sub-vertical down-welling between depths of 100 to 400 km as suggested by earlier work which was restricted by a priori assumptions of crustal structure and essentially a 2-D inversion (Tilman et al., 2003; Kumar et al., 2006). A sub-horizontal orientation of underthrust Indian mantle lithosphere is consistent with positive

buoyancy of a chemically refractory Indian mantle lithosphere – otherwise all shields are expected to have sunk to several kilometers below sea-level due to prolonged cooling since the Archean (e.g., Jordan, 1988). In addition, inefficient propagation of head-waves in the uppermost mantle (Beghoul et al., 1993), large S–P travel-time residuals observed at teleseismic distances (Molnar and Chen, 1984), and deviation from crustal isostasy (Owens and Zandt, 1997; Tseng et al., 2009) all point to an unusually warm upper mantle beyond the IMF. High temperatures, combined with continual northward advance of the IMF, form a condition conducive to E–W ductile flow which, in turn, probably caused large values of  $\delta t$  (Owens and Zandt, 1997; Jimenez-Munt et al., 2008).

### 3. Regional synthesis and tectonic implications

Figs. 5 and 6 compare three N–S trending cross-sections, representing all known large-scale, systematic studies of SKS/SKKS splitting in Tibet. To ensure that exactly the same analysis applies to all three profiles, we re-analyzed all available data in the public domain for the GT and INDEPTH-III profiles. After stacking, which was not applied by the earlier authors, our results have reduced uncertainties but the overall pattern of  $\delta t$  remain unchanged.

Between the two long profiles, Hi-CLIMB and GT (Fig. 6a and c), there is excellent correspondence of all key features in  $\delta t$ . First, null splitting, indistinguishable from that observed over Indian shield in the foreland of the Himalayas, extends to about 100 km north of the IYS. By establishing the pattern of null splitting in underthrust Indian shield as a baseline, one not only has a straightforward explanation for null splitting observed in southern Tibet, but also can identify the onset of significant splitting as the southern limit of Eurasian mantle lithosphere, or the mantle suture – the second notable feature in both profiles. Third, about 100 km north of the Bangong–Nujiang suture (BNS), there is a second marked increase in  $\delta t$ , identified as the Indian mantle front (IMF) (Jin et al., 1996; Chen and Özalaybey, 1998).

The last feature is also apparent along the INDEPTH-III profile (Huang et al., 2000), with values of  $\delta t$  holding steady near the BNS, dropping to a local minimum before jumping up to close to 1.5 s (Fig. 6b). Although Huang et al. (2000) interpret the IMF to lie south of the BNS and did not provide an explanation for this feature, the consistency of this feature among all three profiles is difficult to dismiss (Fig. 6a–c). As such, we are confident about the notion that the IMF, or the northern edge of “Greater India,” in general extends beyond or near the BNS over a lateral (E–W) distance of about 600 km across Tibet. This conclusion is corroborated by consistent result from both P- and S-wave tomography (Hung et al., 2010).

In much of the Lhasa terrane, significant birefringence is curiously missing along the INDEPTH-III profile. Since the onset of significant splitting along this profile is more than 150 km from the identified position of the MS, this jump in  $\delta t$  probably is not related to the MS. An independent marker for the MS comes from the regional distribution of the isotopic ratio  $^3\text{He}/^4\text{He}$ . Along both INDEPTH-III and GT profiles,  $^3\text{He}/^4\text{He}$  ratio drops by an order of magnitude near the position of MS shown in Figs. 5 and 6 (Hoke et al., 2000), consistent with our interpretation of where Eurasian lithospheric mantle terminates which is corroborated by modeling of gravity profiles (Jin et al., 1996; Jjiang et al., 2004).

The origin of null birefringence along the southern portion of the INDEPTH-III profile remains unclear. Additional coverage provided by the regional (lateral) array of Hi-CLIMB shows that between longitudes 85°E and 91°E, null birefringence dominates southern Tibet and extend to about 100 km north of the IYS (Fig. 5). Farther northward, significant birefringence exists both along the GT profile just to the east of 91°E, and along the Hi-CLIMB profile. Puzzling, isolated patches of null birefringence have also been reported in the Western Cordillera of North America (e.g., Savage, 1999). Lately,

West et al. (2009) interpreted one such case under the Great Basin as sub-vertical down-welling in the mantle. However, a similar interpretation for the case at hand is inconsistent with the latest, high-resolution results of tomography (Hung et al., 2010). At this juncture, east–west coverage of geophysical data in Tibet is insufficient to confidently discern if significant lateral variations exist at depth.

Finally south of the BNS (near latitude 32°N), three to four stations show a local peak in  $\delta t$ . This feature is apparent along both the Hi-CLIMB and INDEPTH-III profiles, while station spacing along the GT profile is too sparse to detect such a short-wave-length change (Fig. 6). Given the tight station spacing along these two profiles, Fresnel zones of SKS phase at neighboring stations overlap at depths of about 120 km or less, suggesting that the local feature has its origin in the crust (Alsina and Snieder, 1995); and this feature correlates with the center of a modest anomaly of low  $P$ - and  $S$ -wave speeds detected from the latest travel-time tomography (Hung et al., 2010). A number of studies reported crustal anisotropy in Tibet, including locations along the GT and INDEPTH-III profiles (McNamara et al., 1994; Sherrington and Zandt, 2004; Ozacar and Zandt, 2004; Shapiro et al., 2004), but there is no consistency in estimates of  $\delta t$  (less than 0.2 s up to 0.6 s), nor a consensus in the causes of crustal anisotropy.

#### 4. Conclusions

Using a uniform procedure for analysis, we determine birefringence of  $S$ -waves by using all SKS/SKKS waveforms in the public domain that were recorded by three long transects across the Tibetan collision zone. New results from Hi-CLIMB in west-central Tibet show two distinct, rapid increases in the amount of birefringence toward the hinterland: (1) Null birefringence (split time,  $\delta t$ , of  $0.1 \pm 0.1$  s), which occurs through much of the Himalayan collision front and persists to about 75 km north of the Indus–Yarlung suture (IYS) in southern Tibet, abruptly increases to a  $\delta t$  of about  $0.8 \pm 0.3$  s. (2) Another marked increase in  $\delta t$  occurs about 100 km farther north of the Bangong–Nujiang suture (BNS) in central Tibet. The same pattern occurs along the profile from Yadong to Golmud (profile GT) in east-central Tibet (Fig. 6a and c).

Along the INDEPTH-III transect (Fig. 6b), situated at about 200 km to the west of Profile GT, the rapid increase in  $\delta t$  north of the BNS is also evident. While interpretations based on birefringence alone are likely to be non-unique, a host of other geophysical constraints, including lateral variations in  $P$ - and  $S$ -wave speeds from finite-frequency, multi-scale travel-time tomography, modeling of plate flexure based on gravity anomalies, all indicate that across a regional scale of 600 km, the northern, leading edge of sub-horizontally advancing Indian lithospheric mantle (IMF or the edge of the “Greater India”) has reached beyond the BNS (Fig. 6).

The rapid change north of the YYS, from null birefringence to significant amount of  $\delta t$ , is interpreted as the southern limit of deformed Eurasian lithospheric mantle (or the mantle suture). While this feature is not covered by the INDEPTH-III profile, which curiously showed null birefringence through much of the Lhasa terrane, independent evidence from rapid increase in He isotopic ratios, bolstered by modeling of gravity anomalies, corroborates this interpretation (Figs. 5 and 6).

The current configuration of sub-continental lithospheric mantle (SCLM) beneath Tibet forms a basis for palinspastic (retro-deformable) reconstruction of this important collision zone on a lithospheric scale — an undertaking already carried out back to about 15 Ma ago by Chen and Tseng (2007) in two-dimensions. The extensive lateral coverage of constraints presented in this study should provide a cornerstone for eventual lithospheric reconstruction in full three-dimensions.

#### Acknowledgements

This work was supported by the U.S. National Science Foundation grants EAR99-09362, EAR05-51995, EAR06-35419 (W.-P.C.), and EAR EAR06-35611 (R.L.N.), the U.S. Air Force contract FA8718-08-C-002 (R.L.N. and W.-P.C.), the National Science Council of Taiwan grants 96-2119-M-002-016 and 97-2745-M-002-011 (S.-H.H.), and the Academia Sinica, Taiwan (B.-S.H.) which provided additional personnel (Wen-Tzong Liang, Chia-Lung Wu, John Lin, and Chun-Chi Liu). Seismic experiments were carried out jointly with Oregon State University (lead by John Nabelek), Chinese Academy of Geological Sciences (lead by Jiang Mei and Heping Su), Nepal Department of Mines and Geology (lead by Soma Sapkota and M. Pandey) and Peking University (lead by John Chen). We thank F. Tilmann and an anonymous reviewer for useful comments on the manuscript, and Zhao-hui Yang (University of Illinois) for help with GIS databases.

#### Appendix A

**Table A.1**  
Summary of SKS/SKKS Birefringence from the Hi-CLIMB array.

Station	Lat. (°N)	Long. (°E)	$\phi$ (°) <sup>a</sup>	$\phi$ min.	$\phi$ max.	$\delta t$ (s) <sup>b</sup>	$\delta t$ min.	$\delta t$ max.
H0080	27.166	84.984	79	58	100	0.3	0.0	0.8
H0120	27.283	84.989	87	67	107	0.6	0.1	1.0
H0190	27.472	85.042	31	12	50	0.9	0.3	1.4
H0210	27.529	85.047	73	58	97	0.6	0.4	0.7
H0230	27.580	85.090	33	19	47	0.6	0.3	0.8
H0330	27.861	85.117	85	76	93	0.7	0.4	0.9
H0350	27.911	85.139	93	84	102	0.9	0.5	1.3
H0380	27.995	85.207	91	76	105	0.8	0.4	1.1
H0390	28.025	85.222	49	28	70	0.5	0.1	1.0
H1030	29.483	85.755	94	90	95	1.0	0.8	1.1
H1040	29.561	85.740	90	78	95	1.0	0.5	1.4
H1090	29.922	85.733	36	31	79	0.6	0.3	0.9
H1110	30.066	85.553	48	37	61	0.5	0.4	0.7
H1130	30.206	85.328	10	5	13	1.0	0.8	1.1
H1150	30.358	85.313	28	25	31	1.3	1.0	1.6
H1160	30.434	85.289	30	27	34	1.5	1.1	1.8
H1170	30.496	85.197	36	32	39	1.3	1.0	1.5
H1180	30.581	85.176	42	34	48	1.0	0.8	1.2
H1190	30.649	85.138	40	33	49	0.9	0.7	1.2
H1200	30.715	85.141	36	31	41	1.2	0.9	1.4
H1210	30.782	85.109	44	35	53	0.8	0.6	1.0
H1220	30.860	85.069	72	44	80	0.8	0.6	1.0
H1230	30.932	85.099	70	61	75	1.0	0.9	1.2
H1240	31.020	85.134	74	70	78	1.0	0.9	1.1
H1250	31.084	84.998	84	80	88	1.1	0.9	1.3
H1260	31.155	85.012	80	74	85	0.9	0.8	1.1
H1270	31.225	85.072	82	77	87	1.0	0.8	1.1
H1280	31.302	85.130	94	92	97	1.1	0.8	1.4
H1290	31.378	85.103	78	64	86	0.8	0.5	1.0
H1300	31.445	85.160	82	78	87	1.0	0.8	1.1
H1310	31.515	85.183	72	52	80	0.7	0.6	0.9
H1320	31.584	85.189	76	63	84	0.7	0.5	0.8
H1330	31.656	85.170	80	67	85	0.7	0.5	0.9
H1340	31.732	85.140	84	76	89	0.9	0.7	1.2
H1350	31.803	85.032	82	73	91	0.7	0.5	1.0
H1360	31.862	84.954	82	71	90	1.0	0.7	1.3
H1370	31.945	84.893	90	84	96	1.3	1.0	1.8
H1380	32.004	84.823	90	85	94	1.5	1.1	1.8
H1390	32.072	84.905	82	74	88	1.4	1.0	1.7
H1400	32.119	84.694	92	89	95	1.5	1.2	1.8
H1405	32.181	84.513	96	91	100	1.0	0.7	1.4
H1410	32.236	84.374	82	34	95	0.6	0.3	1.1
H1415	32.308	84.219	40	29	75	1.0	0.6	1.4
H1421	32.009	83.871	60	32	64	0.6	0.4	0.8
H1422	32.064	83.899	46	29	79	0.4	0.2	0.7
H1423	32.159	83.924	72	28	87	0.4	0.3	0.7
H1430	32.382	84.131	48	66	70	1.0	0.8	1.3
H1440	32.455	84.240	72	46	79	0.9	0.7	1.1
H1450	32.524	84.272	48	39	57	0.9	0.7	1.2
H1460	32.598	84.224	54	47	66	1.0	0.8	1.1

(continued on next page)

Table A.1 (continued)

Station	Lat. (°N)	Long. (°E)	$\phi$ (°) <sup>a</sup>	$\phi$ min.	$\phi$ max.	$\delta t$ (s) <sup>b</sup>	$\delta t$ min.	$\delta t$ max.
H1470	32.667	84.216	72	42	82	0.7	0.6	0.9
H1480	32.747	84.216	70	62	82	0.8	0.6	1.1
H1490	32.822	84.267	76	69	84	0.8	0.6	0.9
H1500	32.895	84.286	82	74	89	0.9	0.7	1.1
H1510	32.949	84.305	82	71	92	0.9	0.6	1.3
H1520	33.027	84.315	80	70	89	0.6	0.5	0.8
H1530	33.119	84.221	76	69	88	0.5	0.3	0.6
H1540	33.194	84.228	70	45	78	0.4	0.3	0.6
H1550	33.264	84.246	82	70	91	0.7	0.4	1.0
H1560	33.307	84.246	92	84	96	1.3	0.8	1.7
H1570	33.422	84.263	88	83	92	1.2	0.9	1.5
H1580	33.533	84.291	94	81	99	1.1	0.6	1.6
H1590	33.628	84.171	98	92	102	1.5	0.9	2.3
H1600	33.750	84.270	90	84	93	1.5	1.1	1.8
H1610	33.858	84.263	92	85	97	1.3	0.9	1.7
H1620	33.966	84.223	92	82	96	1.3	0.8	1.7
T0020	28.171	85.969	76	37	60	0.4	0.3	0.8
T0020	28.171	85.969	76	63	81	0.4	0.3	0.8
T0040	28.164	87.356	174	128	178	0.5	0.3	0.9
T0060	28.156	88.099	132	123	140	0.6	0.5	0.9
T0080	28.257	88.991	148	128	178	0.5	0.3	0.8
T0090	28.269	89.392	164	159	169	0.9	0.7	0.9
T0100	28.432	86.097	76	69	79	0.7	0.5	0.8
T0140	28.536	87.759	138	154	176	0.6	0.4	0.8
T0170	28.839	87.950	150	132	154	0.4	0.3	0.5
T0190	28.893	88.781	118	114	124	0.9	0.6	1.1
T0210	28.903	89.577	144	121	178	0.5	0.3	0.8
T0250	29.145	88.159	148	128	178	0.3	0.2	0.6
T0280	29.430	88.231	128	120	141	0.7	0.4	1.0
T0380	30.442	86.931	80	32	93	0.5	0.3	0.8

<sup>a</sup>Orientation of polarization for the fast-traveling component,  $\phi$ , shown as azimuth from the North, and its bounds at two-standard deviations ( $\phi$  min. and  $\phi$  max.).

<sup>b</sup>Split-time between the fast- and the slow-traveling components, and its bounds at two-standard deviations ( $\delta t$  min.  $\delta t$  max.).

## References

- Alsina, D., Snieder, R., 1995. Small-scale sublithospheric continental mantle deformation: constraints from SKS splitting observations. *J. Geophys. Int.* 123, 431–448.
- Argand, E., 1924. La tectonique de l'Asie. *Int. Geol. Cong. Rep. Sess. 13*, 170–372.
- Beghoul, N., Barazangi, M., Isacks, B., 1993. Lithospheric structure of Tibet and western North America: mechanisms of uplift and a comparative study. *J. Geophys. Res.* 98, 1997–2016.
- Chen, W.-P., Özalaybey, S., 1998. Correlation between seismic anisotropy and Bouguer gravity anomalies in Tibet and its implications for lithospheric structures. *Geophys. J. Int.* 135, 93–101.
- Chen, W.-P., Tseng, T.-L., 2007. Small 660-km seismic discontinuity beneath Tibet implies resting ground for detached lithosphere. *J. Geophys. Res.* 112 (B05309). doi:10.1029/2006JB004607.
- Fu, Y.V., Chen, Y.J., Li, A., Zhou, S., Liang, X., Ye, G., Jin, G., Jiang, M., Ning, J., 2008. Indian mantle corner flow at southern Tibet revealed by shear wave splitting measurements. *Geophys. Res. Lett.* 35 (L02308). doi:10.1029/2007GL031753.
- Hoke, L., Lamb, S., Hilton, D.R., Poreda, R.J., 2000. Southern limit of mantle-derived geothermal helium emissions in Tibet: implications for lithospheric structure. *Earth Planet. Sci. Lett.* 180, 297–308.
- Huang, W.-C., Ni, J.F., Tilmann, F., Nelson, D., Guo, J., Zhao, W., Mechie, J., Kind, R., Saul, J., Rapine, R., Hearn, T.H., 2000. Seismic polarization anisotropy beneath the central Tibetan Plateau. *J. Geophys. Res.* 105, 27,979–27,989.
- Hung, S.-H., Chen, W.-P., Chiao, L.-Y., Tseng, T.-L., 2010. First multi-scale, finite-frequency tomography illuminates 3-D anatomy of the Tibetan plateau. *Geophys. Res. Lett.* 37. doi:10.1029/2009GL041875.
- Jiang, X.D., Jin, Y., McNutt, M.K., 2004. Lithospheric deformation beneath the Altyn Tagh and West Kunlun faults from recent gravity surveys. *J. Geophys. Res.* 109, B05406. doi:10.1029/2003JB002444.
- Jimenez-Munt, I., Fernandez, M., Verges, J., Platt, J.P., 2008. Lithosphere structure underneath the Tibetan Plateau inferred from elevation, gravity and geoid anomalies. *Earth Planet. Sci. Lett.* 267 (1–2), 276–289.
- Jin, Y., McNutt, M.K., Zhu, Y., 1996. Mapping the descent of Indian and Eurasian plates beneath the Tibetan Plateau from gravity anomalies. *J. Geophys. Res.* 101 (5), 11,275–11,290.
- Jordan, T.H., 1988. Structure and formation of the continental tectosphere: *J. Petrol., Special Lithosphere Issue*, pp. 11–37.
- Kumar, P., Yuan, X., Kind, R., Ni, J., 2006. Imaging the colliding Indian and Asian lithospheric plates beneath Tibet. *J. Geophys. Res.* 111 (B06308). doi:10.1029/2005JB003930.
- Long, M.D., 2009. Complex anisotropy in D" beneath the eastern Pacific from SKS–SKKS splitting discrepancies. *Earth Planet. Sci. Lett.* 283, 181–189.
- McNamara, D.E., Owens, T.J., Silver, P.G., Wu, F.T., 1994. Shear wave anisotropy beneath the Tibetan Plateau. *Journal of Geophysical Research* 99 (B7), 13,655–13,665.
- Molnar, P., Chen, W.-P., 1984. S–P travel time residuals and lateral inhomogeneity in the mantle beneath Tibet and the Himalaya. *J. Geophys. Res.* 89, 6911–6917.
- Owens, T.J., Zandt, G., 1997. Implications of crustal property variations for models of Tibetan Plateau evolution. *Nature (London)* 387 (6628), 37–43.
- Ozacar, A.A., Zandt, G., 2004. Crustal seismic anisotropy in central Tibet: implications for deformational style and flow in the crust. *Geophys. Res. Lett.* 31 (L23601). doi:10.1029/2004GL021096.
- Özalaybey, S., Chen, W.-P., 1999. Frequency-dependent analysis of SKS/SKKS waveforms observed in Australia: evidence for null birefringence. *Phys. Earth Planet. Interior* 114, 197–210.
- Savage, M., 1999. Seismic anisotropy and mantle deformation: what have we learned from shear wave splitting? *Rev. Geophys.* 37, 65–106.
- Sella, G.F., Dixon, T.H., Mao, A., 2002. REVEL: a model for recent plate velocities from space geodesy. *J. Geophys. Res.* 107 (B4). doi:10.1029/2000JB000033.
- Shapiro, N.M., Ritzwoller, M.H., Molnar, P., Levin, V., 2004. Thinning and flow of Tibetan crust constrained by seismic anisotropy. *Science* 305 (5681), 233–236.
- Sherrington, H.F., Zandt, G., 2004. Crustal fabric in the Tibetan plateau based on waveform inversions for seismic anisotropic parameters. *J. Geophys. Res.* 109 (B02312). doi:10.1029/2002JB002345.
- Silver, P.G., 1996. Seismic anisotropy beneath the continents: probing the depths of geology. *Ann. Rev. Earth Planet. Sci.* 24, 385–432.
- Silver, P.G., Chan, W.W., 1991. Shear wave splitting and sub-continental mantle deformation. *J. Geophys. Res.* 96, 16,429–16,454.
- Tapponnier, P., Xu, Z., Roger, F., Meyer, B., Arnaud, N., Wittlinger, G., Yang, J., 2001. Oblique stepwise rise and growth of the Tibet Plateau. *Science* 294 (5547), 1671–1677.
- Tilmann, F., Ni, J., INDEPTH III Seismic team, 2003. Seismic imaging of the downwelling Indian lithosphere beneath central Tibet. *Science* 300 (5624), 1424–1427.
- Tseng, T.-L., Chen, W.-P., Nowack, R.L., 2009. Northward thinning of Tibetan crust revealed by virtual seismic profiles. *Geophys. Res. Lett.* 36 (L24304). doi:10.1029/2009GL040457, 2009.
- West, J.D., Fouch, M.J., Roth, J.B., Elkins-Tanton, L.T., 2009. Vertical mantle flow associated with a lithospheric drip beneath the Great Basin. *Nature Geosci.* 2, 439–443. doi:10.1038/NAGE0526.
- Wolfe, C.J., Silver, P.G., 1998. Seismic anisotropy of oceanic upper mantle: shear wave splitting methodologies and observations. *J. Geophys. Res.* 103, 749–771.
- Yin, A., Harrison, T.M., 2000. Geologic evolution of the Himalayan–Tibetan orogen. *Ann. Rev. Earth Planet. Sci.* 28, 211–280.